Physics   College of Arts & Sciences

11-2019

Soft X-ray spectroscopy with transition-edge sensors at Stanford Synchrotron Radiation Lightsource beamline 10-1

Sang-Jun Lee

Charles J. Titus

Roberto Alonso Mori

Michael L. Baker

Douglas A. Bennett

See next page for additional authors

Recommended Citation

Authors

Sang-Jun Lee, Charles J. Titus, Roberto Alonso Mori, Michael L. Baker, Douglas A. Bennett, Hsiao-Mei Cho, William B. Doriese, Joseph W. Fowler, Kelly J. Gaffney, Alessandro Gallo, Johnathon D. Gard, Gene C. Hilton, Hoyoung Jang, Young Il Joe, Christopher J. Kenney, Jason Knight, Thomas Kroll, Jun-Sik Lee, Dale Li, Donghui Lu, Ronald Marks, Michael P. Minitti, Kelsey M. Morgan, Hirohito Ogasawara, Galen C. O'Neil, Carl D. Reintsema, Daniel R. Schmidt, Dimosthenis Sokaras, Joel N. Ullom, Tsu-Chien Weng, Christopher Williams, Betty A. Young, Daniel S. Swetz, Kent D. Irwin, and Dennis Nordlund

Soft X-ray spectroscopy with transition-edge sensors at Stanford Synchrotron Radiation Lightsource beamline 10-1 ⊘

Sang-Jun Lee ; Charles J. Titus ; Roberto Alonso Mori; Michael L. Baker; Douglas A. Bennett ; Hsiao-Mei Cho; William B. Doriese ; Joseph W. Fowler; Kelly J. Gaffney; Alessandro Gallo; Johnathon D. Gard ; Gene C. Hilton; Hoyoung Jang; Young Il Joe; Christopher J. Kenney; Jason Knight; Thomas Kroll; Jun-Sik Lee; Dale Li; Donghui Lu; Ronald Marks; Michael P. Minitti ; Kelsey M. Morgan ; Hirohito Ogasawara ; Galen C. O'Neil ; Carl D. Reintsema; Daniel R. Schmidt; Dimosthenis Sokaras ; Joel N. Ullom; Tsu-Chien Weng; Christopher Williams; Betty A. Young; Daniel S. Swetz; Kent D. Irwin ; Dennis Nordlund

Check for updates

⤓ CHORUS

View Online

Export Citation

Articles You May Be Interested In

Solution phase high repetition rate laser pump x-ray probe picosecond hard x-ray spectroscopy at the Stanford Synchrotron Radiation Lightsource

Struct. Dyn. (October 2023)

A seven-crystal Johann-type hard x-ray spectrometer at the Stanford Synchrotron Radiation Lightsource

Rev. Sci. Instrum. (May 2013)

A new μ -high energy resolution fluorescence detection microprobe imaging spectrometer at the Stanford Synchrotron Radiation Lightsource beamline 6-2

Rev. Sci. Instrum. (August 2022)

Soft X-ray spectroscopy with transition-edge sensors at Stanford Synchrotron Radiation Lightsource beamline 10-1

View Online   Export Citation   CrossMark

Sang-Jun Lee,[1,a] iD Charles J. Titus,[2] iD Roberto Alonso Mori,[1] Michael L. Baker,[2,b] Douglas A. Bennett,[3] iD
Hsiao-Mei Cho,[1] William B. Doriese,[3] iD Joseph W. Fowler,[3] Kelly J. Gaffney,[1] Alessandro Gallo,[1]
Johnathon D. Gard,[3] iD Gene C. Hilton,[3] Hoyoung Jang,[1,c] Young Il Joe,[3] Christopher J. Kenney,[1] Jason Knight,[1]
Thomas Kroll,[1] Jun-Sik Lee,[1] Dale Li,[1] Donghui Lu,[1] Ronald Marks,[1] Michael P. Minitti,[1] iD
Kelsey M. Morgan,[3] iD Hirohito Ogasawara,[1] iD Galen C. O'Neil,[3] iD Carl D. Reintsema,[3] Daniel R. Schmidt,[3]
Dimosthenis Sokaras,[1] iD Joel N. Ullom,[3] Tsu-Chien Weng,[1,d] Christopher Williams,[2] Betty A. Young,[4]
Daniel S. Swetz,[3] Kent D. Irwin,[1,e] iD and Dennis Nordlund[1]

AFFILIATIONS

[1] SLAC National Accelerator Laboratory, Menlo Park, California 94025, USA
[2] Stanford University, Stanford, California 94305, USA
[3] National Institute of Standards and Technology, Boulder, Colorado 80305, USA
[4] Santa Clara University, Santa Clara, California 95053, USA

[a] **Email:** sangjun2@slac.stanford.edu
[b] **Current address:** The School of Chemistry, The University of Manchester, M13 9PL Manchester, United Kingdom and The University of Manchester at Harwell, Didcot OX11 0FA, United Kingdom.
[c] **Current address:** PAL-XFEL, Pohang Accelerator Laboratory, Gyeongbuk 37673, South Korea.
[d] **Current address:** School of Physical Science and Technology, ShanghaiTech University, 393 Middle Huaxia Road, Pudong, Shanghai 201210, China.
[e] **Also at:** Stanford University, Stanford, California 94305, USA.

ABSTRACT

We present results obtained with a new soft X-ray spectrometer based on transition-edge sensors (TESs) composed of Mo/Cu bilayers coupled to bismuth absorbers. This spectrometer simultaneously provides excellent energy resolution, high detection efficiency, and broadband spectral coverage. The new spectrometer is optimized for incident X-ray energies below 2 keV. Each pixel serves as both a highly sensitive calorimeter and an X-ray absorber with near unity quantum efficiency. We have commissioned this 240-pixel TES spectrometer at the Stanford Synchrotron Radiation Lightsource beamline 10-1 (BL 10-1) and used it to probe the local electronic structure of sample materials with unprecedented sensitivity in the soft X-ray regime. As mounted, the TES spectrometer has a maximum detection solid angle of 2×10^{-3} sr. The energy resolution of all pixels combined is 1.5 eV full width at half maximum at 500 eV. We describe the performance of the TES spectrometer in terms of its energy resolution and count-rate capability and demonstrate its utility as a high throughput detector for synchrotron-based X-ray spectroscopy. Results from initial X-ray emission spectroscopy and resonant inelastic X-ray scattering experiments obtained with the spectrometer are presented.

Published under license by AIP Publishing. https://doi.org/10.1063/1.5119155

I. INTRODUCTION

Soft X-ray spectroscopy is a powerful probe of local electronic structure that is particularly well suited for studying light-element and 3d transition-metal atoms in a broad range of scientific contexts. One of the most prominent soft X-ray spectroscopy techniques, X-ray absorption spectroscopy (XAS), can provide element, site, symmetry, and spin selective information on the

electronic structure of the samples studied. The technique has been extensively developed and applied to numerous outstanding problems involving transition-metal-centered compounds[1] and light elements.[2] The core-hole-governed element specificity is particularly useful for studying lower concentrations of one element in a larger matrix, such as active metal centers in bioenzymes,[3] minority active sites/intermediates in in-operando catalysis,[4] interfacial transformations during in-operando energy storage,[5] and ultralow concentration of defects and dopants in semiconductors[6–8] and other materials. However, in the soft X-ray regime, the core-hole decay is dominated by nonradiative processes, in particular, Auger transitions, and only ~1% of the decays are radiative. The high yield of Auger and secondary electrons and the ability to attain both high energy resolution and large solid angles in electron detection[9] have driven total-electron-yield XAS (TEY-XAS) and partial-electron-yield XAS (PEY-XAS) and other electron-detected spectroscopies to dominate in the soft X-ray regime. Nevertheless, the powerful insights that can be gained through studying radiative decays, both in the direct decay channels via X-ray emission spectroscopy (XES) and through inelastic loss analysis, e.g., resonant inelastic X-ray scattering (RIXS), have attracted interest over the past decades as high intensity 3rd- and 4th-generation lightsources have come online. These facilities have allowed detailed electronic-structure characterizations of condensed-matter phenomena such as element-specific excitations of spins and magnons,[10] mapping of partial density of states of catalytically relevant adsorbates,[11,12] spin dynamics, and chemical-bond breaking and formation in solution.[13]

Traditionally, XES and RIXS studies via photon-based detection have been performed by wavelength-dispersive method utilizing grazing-incidence diffraction-grating spectrometers,[14] which has a low efficiency but outperform other technologies in terms of energy resolution. There have been continuous efforts to increase the efficiency of spectrometers using variable line spacing (VLS) gratings,[15] reflection zone plates (RZPs),[16,17] transmission Fresnel zone plates (FZPs),[18] or some other X-ray optics.[19] Although significant improvements have been made in terms of the acceptance angle, these methods have not yet been demonstrated to simultaneously provide high energy resolution and high efficiency that is sufficient for RIXS measurements of ultra-low-concentration (sub-millimolar) samples.

To address the need for a spectrometer with greater sensitivity, we have developed and successfully commissioned an energy-dispersive soft X-ray spectrometer based on transition-edge sensors (TESs) composed of Mo/Cu bilayers[20,21] at the Stanford Synchrotron Radiation Lightsource (SSRL) beamline 10-1 (see Fig. 1). The TES spectrometer has a demonstrated full-array energy resolution of 1.4 eV at 250 eV and 1.5 eV at 500 eV. This spectrometer provides 2×10^{-3} sr collection solid angle and ~0.2 detection efficiency. As a comparison, these parameters are, respectively, about 10 and 3 times better than those of high-throughput VLS grating spectrometers.[22,23] The TES array also offers ~50 times better energy resolution than Fano-limited silicon drift detectors.[24] The energy-dispersive nature of the TES brings another big advantage; its energy resolution is not affected by the beam size on
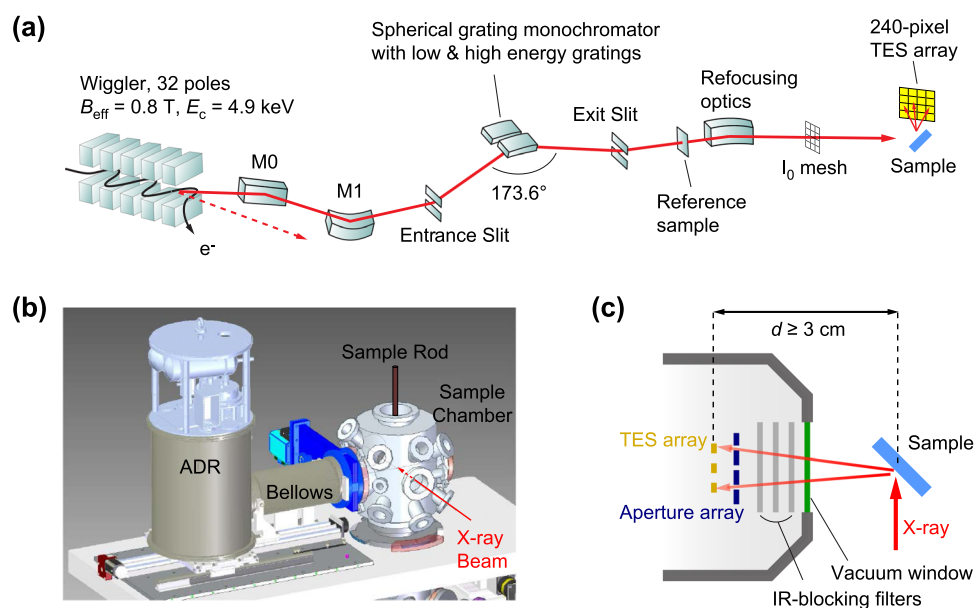

FIG. 1. (a) Schematic diagram of beamline 10-1 at SSRL (BL 10-1). The dashed red arrow indicates the direction of the central cone of the synchrotron radiation. M0 and M1 are X-ray optics. (b) 3-dimensional rendering of the TES end-station at BL 10-1. The TES array is mounted at the end of a horizontal cold finger that is thermally anchored to the coldest stage of an adiabatic demagnetization refrigerator (ADR). Samples are placed in the path of the X-ray beam using a vertical load lock chamber (not shown) and a 4-axis manipulator. The samples are thermally and mechanically decoupled from the TES array. The XPS measurement system (not shown) is located on opposite sides of the main chamber from the TES. (c) Simplified view (not to scale) of the sample-region geometry. The (leftmost) yellow bars, thick dark blue bars, three light gray bars, and one green bar represent the 240-pixel TES array, the X-ray aperture array, three successive IR-blocking filters at 60 mK, 2.7 K, and 50 K, and a vacuum X-ray window at room temperature, respectively. The filters and the window are commercially available from Luxel Co. The minimum achievable distance from the TES array to the center of the sample is $d \approx 3$ cm.

samples. Thus, a large defocused beam can be used to minimize radiation damage on the sample without degrading the detector performance. These capabilities enable higher-throughput experiments with expanded scientific reach. This paper outlines the performance of the TES spectrometer as deployed at beamline 10-1 of SSRL.

II. OVERVIEW OF BEAMLINE 10-1

The TES spectrometer is attached to the soft-X-ray spectroscopy end-station of beamline 10-1 of SSRL (BL 10-1). A schematic diagram of the beamline is shown in Fig. 1(a). BL 10-1 is a mature experimental station that has been optimized for high-throughput measurements. It offers an assortment of X-ray absorption detectors as well as photoemission capabilities. The main experimental chamber at BL 10-1 is equipped with a PHI 15-255GAR double-pass cylindrical mirror analyzer (CMA) for X-ray photoelectron spectroscopy (XPS), a Channeltron electron multiplier from Photonis for TEY-XAS or PEY-XAS, an IRD AXUV-100 Si

photodiode for total-fluorescence-yield XAS (TFY-XAS), and empty ports aligned to the interaction point that can accommodate other detectors (such as our TES array). As shown in Figs. 1(b) and 1(c), the TES array is located perpendicular to the incident beam in the horizontal plane. The other detectors have been placed in the forward (upstream) part of the chamber. The top chamber has accommodations for surface-science preparations, including evaporators, and is equipped with a gas-inlet leak valve, a residual-gas analyzer (RGA 100 from SRS), and a quartz-crystal microbalance (QCM) thickness monitors.

Beamline 10-1 is downstream from a 32-pole, 1.27-T wiggler magnet ($B_{center} \approx 0.81$ T) that generates a broadband spectrum of X-rays with approximately 80% linear polarization and a critical photon energy of 4.85 keV. The acceptance angle for BL 10-1 is 1.0 mrad (horizontal) × 0.84 mrad (vertical) with the centerline at 2.0 mrad (horizontal). The beamline has a spherical-grating monochromator (SGM) with two interchangeable gratings mounted in a Rowland configuration with a movable entrance slit. One grating, with 600 lines/mm, provides monochromatic X-rays in the
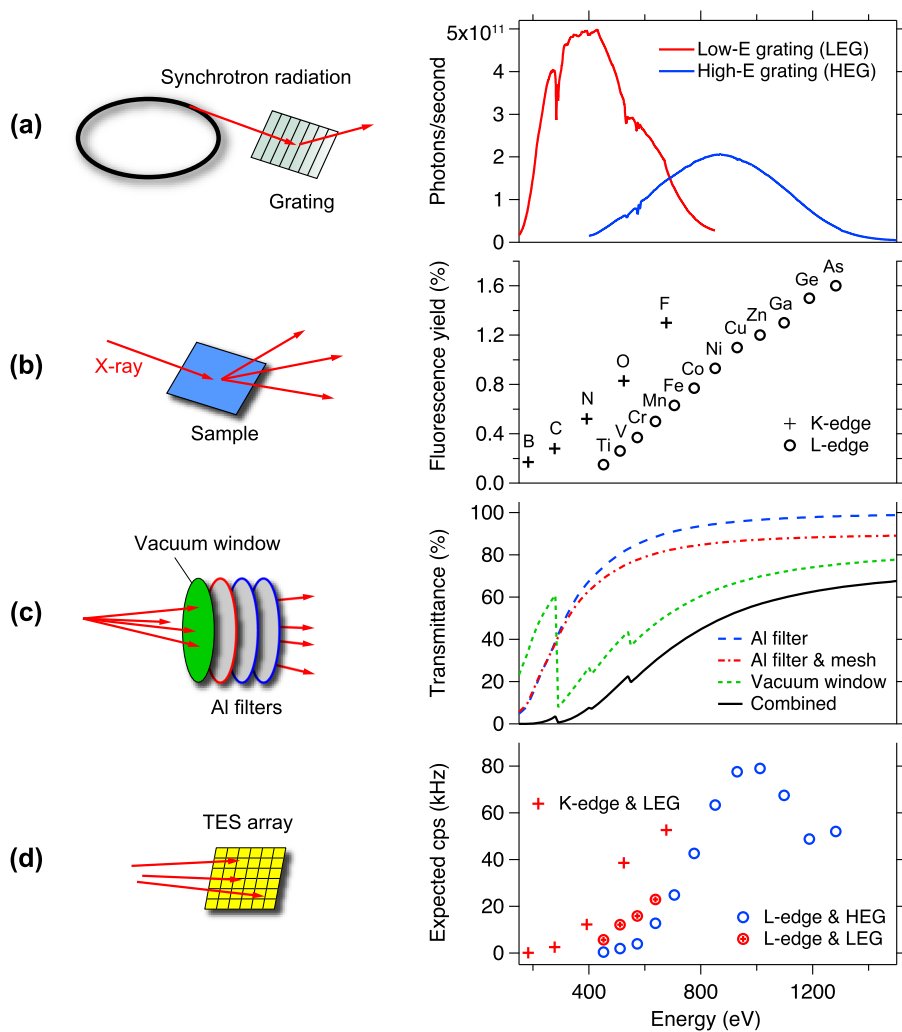

FIG. 2. (a) Measured number of photons/s as a function of beam energy for the two gratings at BL 10-1, with beam entrance and exit slit openings of 40 μm. The estimated resolving powers ($E/\Delta E_{FWHM}$) of monochromatic X-ray beam with the slit openings of 40 μm are 1600 for LEG and 2300 for HEG, and roughly scale with the inverse of the sizes of the slit openings. Sharp features near 280 eV and 530 eV are due to absorption of X-rays by C and O contaminants, primarily carbonyls on mirror surfaces. (b) Literature values for fluorescence yield of the K-edge decay from light elements and the L-edge decay from 3d transition metals and other period-4 elements.[25] (c) Theoretical transmittance of: a vacuum X-ray window, a uniform 113-nm-thick Al filter, a 102-nm-thick Al filter on a Ni mesh with 10% fill factor, and the combined stack of the vacuum window and all three filters. Measured transmittance curves (not shown) for each filter were in good agreement with the theoretical values. (d) Predicted X-ray counts per second (cps) at the TES detector array, taking into account filter transmittance, for a sample-to-array distance of 4.5 cm, and assuming 100% concentration for each element noted in (b).

energy range 200–600 eV. The second, with 1000 lines/mm, covers 500–1300 eV [see Fig. 2(a)]. The monochromatic beam is refocused at the X-ray–sample interaction point by a toroidal mirror, adjustable to yield on-sample spot sizes approximately from 0.7×0.7 mm^2 to 1.5×1.5 mm^2 under normal operating conditions. The maximum energy-resolving power of the beam is $E/\Delta E_{FWHM} \sim 5000$. A small fraction (~2%) of the beam is intercepted upstream of the refocusing mirror by a reference sample consisting of a set of thin-film transition-metal oxides that, including carbon contamination and higher-order contributions, offers distinct energy-calibration features every 50–100 eV throughout the operating range. The intensity (I_0) of the incident beam is monitored via a drain current from an electrically isolated mesh with evaporated gold (typically in the order of a few hundred pA), providing a clean measure of the beam intensity that is used for normalization and to estimate the absolute flux (separately calibrated by a photodiode).

Samples are typically mounted onto the sides of an aluminum square rod ($1.9 \times 1.9 \times 11.4$ cm^3) that allows an effective total mounting area greater than 100 cm^2. The samples can be heated to ~1000 K or cooled to ~50 K *in situ*. Using liquid nitrogen to cool the sample rod to ~80 K is routine. The sample-mounting rod is attached to the bottom of a 4-axis manipulator (Omniax from VAC-GEN) with a positioning system, developed in-house, that provides 3-dimensional sample-position accuracy of ±100 μm when used with standard calibration procedures. Once the calibration is completed, the computer-controlled positioning system allows hundreds of samples to be automatically placed at the desired beam interaction point. Each sample can be measured with a variety of detectors without user interaction. The sample-mounting rod is electrically isolated from the sample chamber via a sapphire plate, which allows for sample drain currents to be measured as an additional TEY-XAS yield. A load-lock system allows large sets of samples to be exchanged into and out of high-vacuum conditions in less than an hour for low-degassing samples.

In summary, SSRL BL 10-1 provides a powerful platform for a wide range of soft-X-ray spectroscopy applications. The high degree of automation at BL 10-1 enables data acquisition from hundreds of samples with no user intervention. The state-of-the-art TES-based spectroscopy described in this work, coupled with conventional XAS and XPS, enables high sample throughput and unique capabilities in the soft X-ray regime for XAS, XES, and RIXS.

III. OVERVIEW OF THE TES SPECTROMETER

The heart of the TES spectrometer is a 240-pixel array of microcalorimeters.[21] Each pixel in the TES array is a separate thermal sensor that transduces the energy deposited by individual X-rays into current pulses. Each pixel consists of a Mo/Cu TES deposited on a silicon nitride membrane and covered by a $124 \times 124 \times 2.8$ μm^3 Bi absorber that provides near-unity quantum efficiency for X-rays up to 1.5 keV. Each pixel is masked by a 104×84 μm^2 aperture to ensure that incident X-rays are not absorbed in the interstitial regions of the TES array. Out of the total 240 pixels in our array, 222 pixels are active (92.5% yield), which translates into a maximum detection solid angle of 2×10^{-3} sr for the whole array, subtended by the apertures at a sample-to-array distance of 3.0 cm. The TES array is mounted at the end of a cold finger that is thermally anchored to the

cold stage of an adiabatic demagnetization refrigerator (ADR) and protrudes into the sample chamber at a 90° angle with respect to the incident X-ray beam, as shown in Fig. 1. The TES array is separated from the sample chamber by a vacuum-holding X-ray window at room temperature and three IR-blocking filters mounted at sequentially lower temperature stages of the cryostat. The two innermost IR filters are 110-nm-thick, freestanding Al films that are separately mounted inside the ADR at 60 mK and 2.7 K. The third filter, a 100-nm-thick Al film, backed by a Ni mesh (10% fill factor), is mounted at 50 K. Without the three filters, IR loading would keep the TES array from cooling to its operating temperature. The filter thicknesses were chosen to maximize the transmittance in the soft X-ray band while keeping the transmittance in the IR band to an acceptable level. The transmittance curves of the vacuum window and the two types of Al filters (with and without mesh) are shown in Fig. 2(c), along with the combined filter transmittance. Expected total count rates of the TES for common elements in the soft X-ray regime based on beam flux, fluorescence yield, and the transmittance are shown in Fig. 2(d). In principle, the outermost vacuum window could be removed before a run to achieve even higher collection efficiency for extremely dilute and/or damage sensitive samples. This option is currently not in use due to vacuum safety and risk mitigation reasons.

Each superconducting Mo/Cu TES in the microcalorimeter array has a critical temperature $T_c \approx 107$ mK, with a steep superconducting-to-normal transition, making the TESs highly sensitive to small temperature changes. The TES chip is cooled to well below the T_c of the devices using a commercial ADR that is temperature regulated at 60 mK with $\sigma = 6$ μK stability. At this temperature, the system provides ~30 h of measurement time. A small bias voltage is used to simultaneously maintain each TES in its superconducting-to-normal transition. When an X-ray is stopped by one of the Bi absorbers, the photon energy E_X is deposited in the absorber and the pixel undergoes a small temperature rise before cooling back to its quiescent temperature [see Fig. 3(a)].

The small pixel heat capacity (~1 pJ/K) ensures that even a small amount of absorbed energy results in a precisely measurable increase in both TES temperature and resistance. The change in resistance causes a change in TES current $|\Delta I_{TES}|$, which is measured with a dc-SQUID (Superconducting Quantum Interference Device) inductively coupled to the TES. In the present detector array, we typically observe 1/e rise-time and decay-time constants of ~70 μs and ~150 μs, respectively, with an additional long decay-time constant of ~500 μs for $E_X \sim 530$ eV (O-K).

Signals from the TES array are multiplexed using a SQUID-based time-domain multiplexing (TDM) technique,[27] the most mature technology used to date to read out large TES arrays.[28] Multiplexed readout is used to reduce the number of cryostat wires needed to connect room temperature electronics to the many-pixel detector array on the cold stage, leading to a manageable heat load. Our 240-channel (pixel) TDM is configured as 30 "rows" × 8 "columns."[29] Detector pixels that are read on the same TDM column are sequentially read out in a switching interval of $T_s = 160$ ns. Pixels on the same row are read out in parallel. The numbers of rows and columns can be adjusted within their maximum parameters of 30 and 8, respectively, using software controls. Decreasing the number of multiplexed pixels modestly improves energy resolution at the cost of collecting area. For instance, as a smaller number of rows, N_{Rows}, is
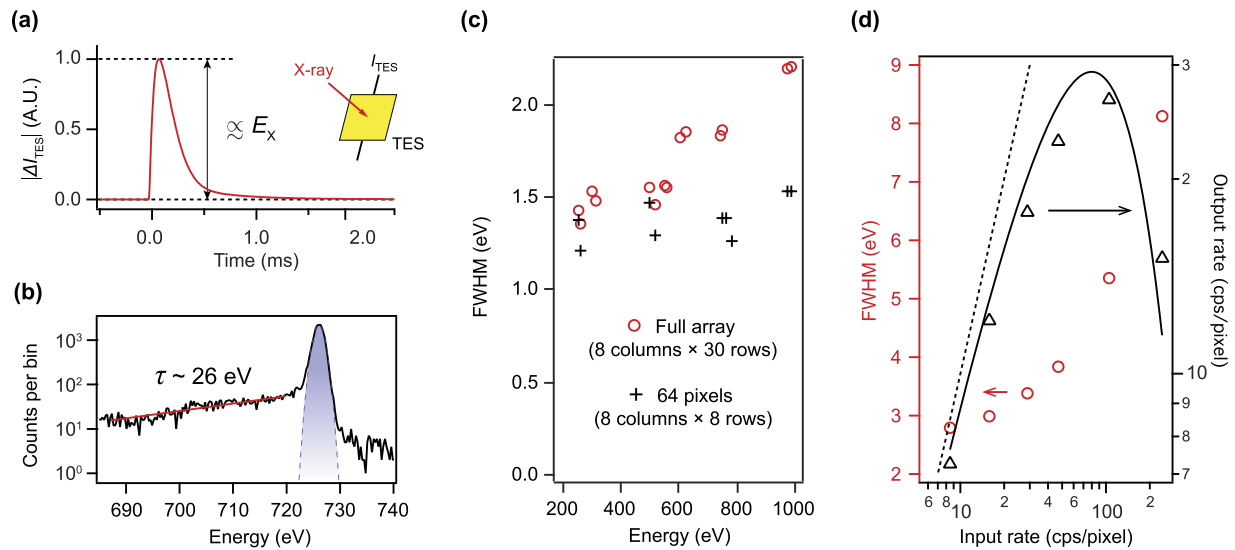
FIG. 3. (a) A typical X-ray signal detected by a single pixel of the TES microcalorimeter array. Absorption of a single X-ray photon induces a pulse in the TES current (I_{TES}) whose height is approximately proportional to the energy of the photon (E_X). (b) Energy-pulse-height spectrum obtained from 20 min of runtime for 220 pixels of the TES array subject to a 726 eV X-ray beam elastically scattered off a Au foil. The spectral shape is primarily Gaussian (blue dashed line) but has a small low-energy tail which exponentially decays with a decay-constant of ~26 eV. (c) Measured TES energy resolution (Gaussian FWHM) as a function of incident X-ray energy for two different SQUID-readout multiplexing factors (N_{Rows} = 8 and 30), corresponding to 64 TES pixels and the full 240-pixel array, respectively. The per-pixel count rate of each data point was in the range of 0.5–2 cps. (d) Observed FWHM of the resonantly excited Cu Lα emission line at ~930 eV for the full TES array (left axis) and output per-pixel count rate (right axis) as a function of input per-pixel X-ray rate. The dashed line is a guide-to-the-eye corresponding to the ideal case where the output rate is equal to the input rate. The solid line is a fit to the data with $r_{out} = r_{in} e^{-r_{in}(t_{rec} + t_{RTB})}$, where r_{out}, r_{in}, t_{rec}, and t_{RTB} are output rate, input rate, record length in time, and "return-to-baseline" time, respectively.[26] The fitting parameter t_{RTB} was found to be ~5.2 ms.

used (i.e., a smaller number of pixels are read out), high-frequency read-out noise beyond the Nyquist frequency is less aliased into the lower-frequency signal band, leading to an improved signal-to-noise ratio.[30,31] This effect will be further discussed in Sec. IV, where we describe X-ray measurements performed using two different multiplexing configurations.

We use custom software to configure detector-readout parameters such as the total number of channels connected, TES and SQUID bias voltages, signal trigger conditions, and the number of samples in a time record of the TES current ("record length"). The data-acquisition software enables real-time monitoring that provides a live map of trigger rates of all pixels, visualization of individual X-ray pulses, pulse height vs time diagnostic plots, and pulse-height distributions for each pixel. The TES spectrometer is integrated with the beamline-control software. For a sufficiently low trigger level, the total trigger rate as a function of incident X-ray energy provides a first-order approximation of total-fluorescence-yield X-ray absorption spectrum (TFY-XAS). TFY-XAS is available in real time and serves as a highly useful diagnostic for properly selecting the TES and beamline parameters for each experiment.

The data stream of multiplexed SQUID signals flows into a data-acquisition PC at a ~100 MB/s rate. Individual X-ray events are captured by a software edge-trigger and written to disk with a fixed total record length and a pretrigger length (typically 1/4 of the total record length). The user can freely choose the total record length and the pretrigger length but since they affect critical detector-performance parameters, there is a finite range of favored

record-length values. More specifically, for typical TES X-ray data, the shorter the record length, the more the detector resolution degrades from its maximum achievable resolution in the low count-rate limit.[26] As the count rate increases, however, more X-ray pulses are rejected due to the pulse pile-up in the standard data processing. Thus, the total record length can be carefully optimized for each measurement to meet the balance between the required energy resolution and the counting rate capability, but in many cases, it is sufficient to use our typical value of ~1500 samples (~7.5 ms) per record, which is long enough so as not to significantly affect energy resolution while providing descent a counting rate. We are currently investigating novel ways to analyze shorter record lengths and maintain excellent energy resolution for individual X-ray pulses. A systematic study of detector performance as a function of both the input X-ray count rate and record length will be reported in a separate paper.

Each X-ray pulse signal is analyzed offline using a Wiener optimal filter, which is known to provide the best estimator of energy of X-ray pulses for TES detectors in the presence of noise.[32,33] The noise spectral density is measured separately without incident X-rays (dark signal) once every ADR cycle (~30 h), at the beginning of base temperature regulation. To enable a practical implementation, the TES noise is assumed to be stationary within the same ADR cycle. Although the temperature of the cryostat is kept constant to within several µK rms, the TES current-signal "baseline" (detector current in the absence of X-rays) often experiences an hour-scale fluctuation or drift that corresponds to as much as ~0.5 eV/h. We use the

pretrigger region of each X-ray pulse to empirically correct for such pulse-to-pulse variations in the signal baseline.[34] Each pixel of the TES spectrometer is individually energy-calibrated at the start of an ADR cycle using a reference sample producing known X-ray lines. Only after each pixel is energy calibrated can a summed spectrum of all live pixels be obtained. TES signal processing will be discussed in more detail in Sec. V.

IV. PERFORMANCE OF THE TES SPECTROMETER

Key characteristics of the TES spectrometer include its energy-response function, gain linearity, energy resolution, and maximum count rate. A typical TES X-ray pulse measured by a single TES of the spectrometer array is shown in Fig. 3(a). Figure 3(b) shows the response to monoenergetic X-rays that is summed over the whole array. As can be seen in the figure, the detector response is mostly Gaussian but has a non-Gaussian component in the form of a low energy tail, which is thought to be due to incomplete thermalization of the X-ray energy that is absorbed in the 2.8-μm-thick evaporated Bi absorbers attached to the TES pixels. Yan *et al.* recently made progress in electroplating Bi absorbers that are free of such low energy tails.[35] We hope to take advantage of this development in a future upgrade of our TES spectrometer.

The energy resolution of the TES spectrometer as a function of energy was obtained by measuring monochromatic X-rays elastically scattered off of a gold film deposited on a silicon wafer. The results are summarized in Fig. 3(c). The detector resolution was calculated by taking the FWHM of the Gaussian part of the measured energy spectrum of the monochromatic X-rays and subtracting the theoretically expected FWHM of the incident X-ray beam in quadrature. The measurement was done with two different multiplexing factors (N_{Rows}) of 8 and 30. An N_{Rows} value of 8 reads out 64 pixels (8×8), while an N_{Rows} value of 30 reads out the whole array (30×8). As can be seen in the Fig. 3(c), $N_{Rows} = 30$ results in non-negligible degradation of the detector energy resolution compared to the case of $N_{Rows} = 8$. The difference can be explained by the increase of SQUID read-out noise by a factor of $\sqrt{N_{Rows}}$, a characteristic of TDM.[30,31] Also to be noted in this plot is the degradation of energy resolution with increasing energy, especially in the case of $N_{Rows} = 30$. The approximately linear trend implies that the main source of degradation is electrical crosstalk between channels whose strength is expected to increase with both mean energy of X-rays and N_{Rows}. This study shows a trade-off between energy resolution and detection efficiency (collecting area), especially at higher energies. Thus, the best strategy is to maximize N_{Rows}, while keeping the energy resolution within the requirement of each experiment.

The count-rate capability of the TES spectrometer is primarily determined by the decay time of X-ray pulses, which is set by the detector design and operating temperature. The time it takes for a TES pixel to return to its quiescent temperature after the absorption of an X-ray varies from pixel to pixel and is typically a few milliseconds. A representative X-ray pulse is shown in Fig. 3(a) that takes ~2.9 ms for the pulse to decay to the 0.1% level of the pulse maximum. A count-rate study of the TES spectrometer was performed using a Cu metal foil mounted at 45° with respect to the incoming monochromatic X-ray beam of ~948 eV. Due to the strong fluorescence yield of the Cu Lα line, the TES was able to detect as many as ~50 000 X-rays/s on the whole array at a sample-to-array distance

of 45 mm. The rate of X-rays impinging on the TES was adjusted by moving the TES spectrometer away from the sample. The input count-rate dependence of the spectral energy resolution and the output count rate for 6 different sample-to-array distances are shown in Fig. 3(d). Output count rate is defined as the number of X-ray pulses per second per pixel that pass basic pile-up and pulse-shape cuts. The input count rate was calculated by counting all the X-ray pulses in each record, including any secondary pile-up pulses. Figure 3(d) can be easily converted to more practical trigger-rate dependence curves using the relation between the trigger rate and input count rate as discussed in the supplementary material. For example, the second-highest input rate of 105 cps/pixel corresponds to a trigger rate of 58 Hz/pixel. As the incoming X-ray flux increases, the energy resolution degrades, mainly due to crosstalk between neighboring pixels. The output count rate initially increases, but then drops for incoming X-ray flux larger than ~60/s/pixel. Note that the exact trends of energy resolution and output rate depend on the details of the cuts used for the data analysis since the level of detector noise and stability can vary.

V. TES ENERGY CALIBRATION AND STREAMLINED DATA-TAKING

We have developed an efficient and streamlined data-acquisition procedure that maximally utilizes the 30-hour-long ADR thermal cycle while minimizing TES systematic errors. The procedure is illustrated in Fig. 4(a). In a single ADR cycle, we record a noise dataset, multiple energy calibration datasets (~20 min each), and science datasets. The noise dataset is taken at the beginning of the ADR cycle, before the X-ray beam is allowed into the sample chamber. 10 s of data acquisition time is sufficient to obtain a smooth noise spectral density used to construct an optimal filter for each pixel.

In the first calibration dataset (Cal$_1$), a monoenergetic X-ray beam is used to fluoresce a reference sample comprised of various elements with known emission-line energies in the range of interest. After initial calibration, measurements of science samples (Sci$_1$, Sci$_2$, ...) are done. Science operation continues for the duration of the ADR cycle, aside from brief interruptions every several hours for additional calibration runs (Cal$_2$, Cal$_3$, ...). These periodic calibrations, performed under the same conditions as the first calibration (Cal$_1$), allow us to compensate for slow temperature fluctuations of the detector system and monitor the energy calibration overall. Further corrections to account for fine-scale energy-gain fluctuations over the entirety of the data run (~10–30 h) are dealt with empirically by tracking common emission lines. Once the temperature fluctuations are corrected, gain curves are created from each pixel in the Cal$_1$ dataset and applied to all the other datasets to convert their optimal-filtered pulse-heights to energy. Because the gain curve is a nonlinear function of pulse-height, we interpolate between the calibration points using a spline, following Fowler *et al.*[36]

During calibration, we typically fix the sample-to-array distance at 4 cm and use beamline monochromator entrance- and exit-slit openings of 50 μm. These conditions yield a total TES array count rate of ~2000 Hz. 20 minutes of data acquisition provides well-defined energy calibration peaks for each TES pixel. The calibration spectrum shown in Fig. 4(b) was obtained using the high-energy grating on BL 10-1 and an incident X-ray energy of 1000 eV. For
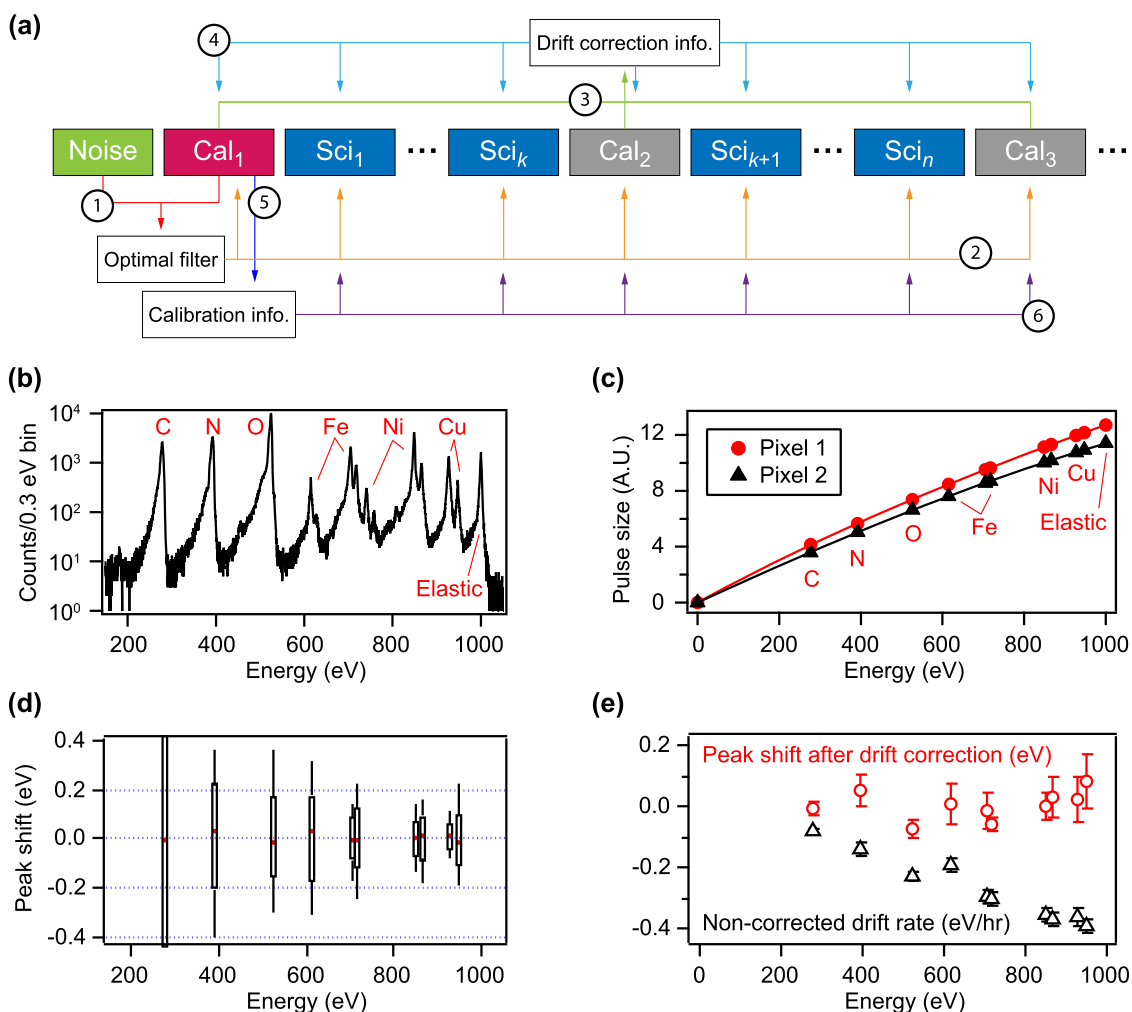
FIG. 4. TES energy calibration: (a) Analysis flow diagram showing the data acquisition procedure during a single ADR thermal cycle. Circled numbers indicate the order of the data processing. The optimal filter is built (①) and applied to all calibration and science data (②). The drift correction information is calculated (③) and applied to all the data (④). The energy-calibration information is calculated (⑤) and applied to all the data (⑥). (b) XES spectrum taken with the TES array (211-pixel spectra combined) and a calibration sample containing several elements excited by an incident 1000 eV X-ray beam. The highest-energy peak corresponds to elastically scattered X-rays at 1000 eV. When energy calibration beyond the Cu emission lines is needed, another calibration sample containing Zn is used. The compositions of two most commonly used calibration samples can be found in the supplementary material. (c) TES gain curve for two pixels, showing generic quartic dependence. The results shown are typical for most pixels of the array. Circles and triangles correspond to calibration points: C-K, N-K, O-K, Fe-Ll, Fe-Lα, Fe-Lβ, Ni-Lα, Ni-Lα, Cu-Lα, Cu-Lβ, obtained using an incident 1000 eV X-ray beam. The points at (0, 0) assume no TES response for zero energy input and the highest-energy points correspond to the incident beam energy. Marker sizes are larger than 0.5% experimental uncertainties. (d) "Leave-one-out cross-validation test"[36] shows a calibration accuracy of better than 0.1 eV. The red dots, black boxes, and whiskers correspond to the median, 25th–75th, and 10th–90th percentiles of pixel-to-pixel distribution at each calibration point, respectively. The box and whisker for the carbon line (not fully shown) span −0.9 to 0.9 eV and −1.7 to 1.6 eV, respectively. (e) Peak-shift rates (black triangles) before gain drift correction and average peak shifts (red circles) after drift correction, obtained from six 12-min measurements of the calibration sample spread over a 4-h period. The first dataset (Cal₁) was used to calibrate all the six datasets, and drift correction information was obtained with the first and the last datasets combined. The error bars for the peak shifts and the peak-shift rates represent the standard deviation of peak shifts and the 1σ fitting error of peak-shift rates.

science measurements that use the low energy grating, we typically excite the multielement calibration sample at ~450 eV. The second harmonic of the low energy grating provides excitation of the oxygen line with sufficient intensity to be useful. The Cal₁ dataset enables us to create a pulse template and a detector gain curve for each pixel. As shown in Fig. 4(c), the gain of individual pixels increases

with energy following a roughly quartic dependence. Pulse templates and measurements of the noise-spectral-density are obtained at the start of every ADR run. This measurement is important because the local magnetic field environment can change from one thermal cycle to the next. Figures 4(d) and 4(e) show the overall accuracy and stability, respectively, of our standard calibration, which are both

good to below 0.1 eV. We are currently refining our measurement and analysis strategy in order to minimize the effects of fine-scale drifts to achieve undegraded accuracy and precision over the entire ADR cycle. More frequent measurements of secondary calibration datasets is considered as a solution for this issue.

VI. PERFORMING XES, XAS, AND RIXS WITH A TES ARRAY

Our TES spectrometer can be used on BL 10-1 for X-ray emission spectroscopy (XES), X-ray absorption spectroscopy (XAS), and resonant inelastic X-ray scattering (RIXS). In an XES measurement, a monochromatic X-ray beam impinges onto the sample with an energy equal to (resonant XES) or greater than (nonresonant XES) the absorption edge to be measured. The TES spectrometer then records X-rays emitted by the sample over the full detector energy sensitivity band. TES-based XES is essentially a static measurement. By contrast, XAS/RIXS measurements are made by systematically sweeping the incident X-ray beam energy across element-specific absorption edges in a sample. In XAS/RIXS, each recorded X-ray event is assigned to a monochromatic incident X-ray energy based on its timestamp.

To demonstrate the high sensitivity and broadband multi-edge XES capability of the TES spectrometer, we show in Fig. 5 the nonresonant emission spectra for two samples: N-doped (~1%) graphene (on Si substrate) and dry photosystem-II (water-plastoquinone oxidoreductase, PS-II), excited by monochromatic X-rays of 440 eV and 1100 eV, respectively. The red highlighted regions in the XES spectra correspond to the N-K and Mn-L emission lines of the samples, respectively. These brief diagnostic measurements took less than an hour and utilized the full TES array with a known energy resolution of 1.5–1.8 eV in this energy range [see Fig. 3(c)]. Even these low-statistics data show how the TES spectrometer can be very effective at measuring weak signals in the presence of substantial background.

For many sample sets, it is important to measure emission-line shifts smaller than the resolution of the TES.[37] Simply increasing measurement time to reduce statistical uncertainties is not sufficient due to detector gain instability. But this limitation can be mitigated by performing XES measurements alternately on multiple samples

in a set, thereby reducing systematic uncertainties in determining the small energy shifts. Initial results obtained with iron-based photosensitizer samples showed the power of this method.[38] The results from these measurements will be reported separately.

When combined with traditional XPS (X-ray photoelectron spectroscopy) overview scans, TES-based XES can provide complementary information about a sample's elemental composition as a function of depth. Conventional XPS can be used to measure sample concentrations as small as 0.5%, but the technique only provides depth information of ~5 nm. By contrast, TES XES can provide <0.1% concentration sensitivity and probes depths up to 50–100 nm.[39]

Also shown in Fig. 6 is the full RIXS plane for a sample of frozen aqueous $K_3[Fe(CN)_6]$ solution. The measurement and analysis for a subset of these data were fully detailed in Ref. 40. In a RIXS measurement, an XES spectrum is obtained at each SGM energy setting. These XES spectra are combined to create a 2-dimensional RIXS plane of sample X-ray emission energy vs incident monochromatic X-ray energy. Partial-fluorescence-yield XAS (PFY-XAS) information can be derived from the RIXS data by summing the X-ray counts in the RIXS map for each monochromatic incident energy, as shown in Fig. 6.

A close look at the L-edge RIXS data of 3d transition metals reveals a powerful capability of the TES spectrometer. As shown in Fig. 6, when a core-hole is created during a RIXS measurement, two modes of fluorescent core-hole decay exist, one corresponding to the dominant $3d \rightarrow 2p$ transition, and the other to $3s \rightarrow 2p$ core-to-core transition. Both transitions are simultaneously measured by the TES due to its broadband spectral coverage. Summing over the two different energy ranges results in two different types of the PFY-XAS spectrum as shown in Fig. 6. Although the $3d \rightarrow 2p$ spectrum has the same overall shape as the true XAS spectrum, the weight of the spectral features can be different because the fluorescence yield depends on the final state angular momentum. As previously reported,[40,41] the $3s \rightarrow 2p$ spectrum is known to better represent the true absorption. Although the $3s \rightarrow 2p$ decay channel has 5–10 times lower intensity than the $3d \rightarrow 2p$ decay, the TES is sensitive enough to provide a high signal-to-background spectrum. Another feature of the TES-based RIXS associated with its broadband coverage is that in some samples, an inverse PFY (IPFY) spectrum can be obtained with
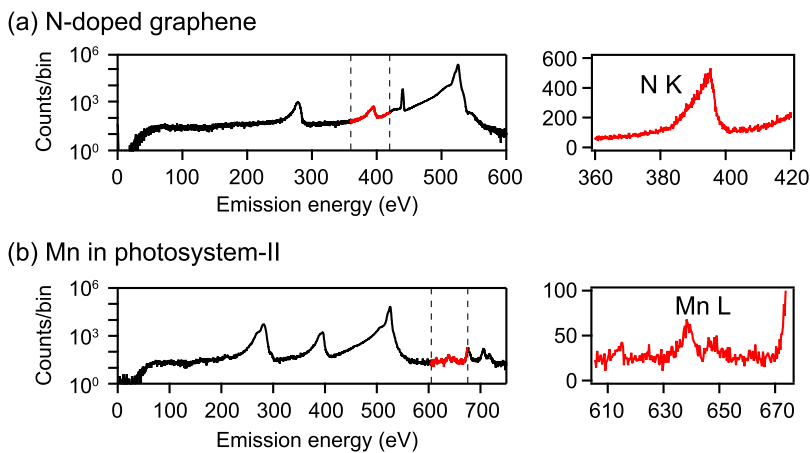
(a) N-doped graphene

(b) Mn in photosystem-II

FIG. 5. XES spectra for (a) low concentration light atoms in a 2-dimensional material (N-doped graphene, ~1% of a monolayer concentration) and (b) low concentration transition metal in a biomatrix (Mn in a dried PS-II). The right figures show magnified views of the region between two dashed lines in the left figures, respectively.
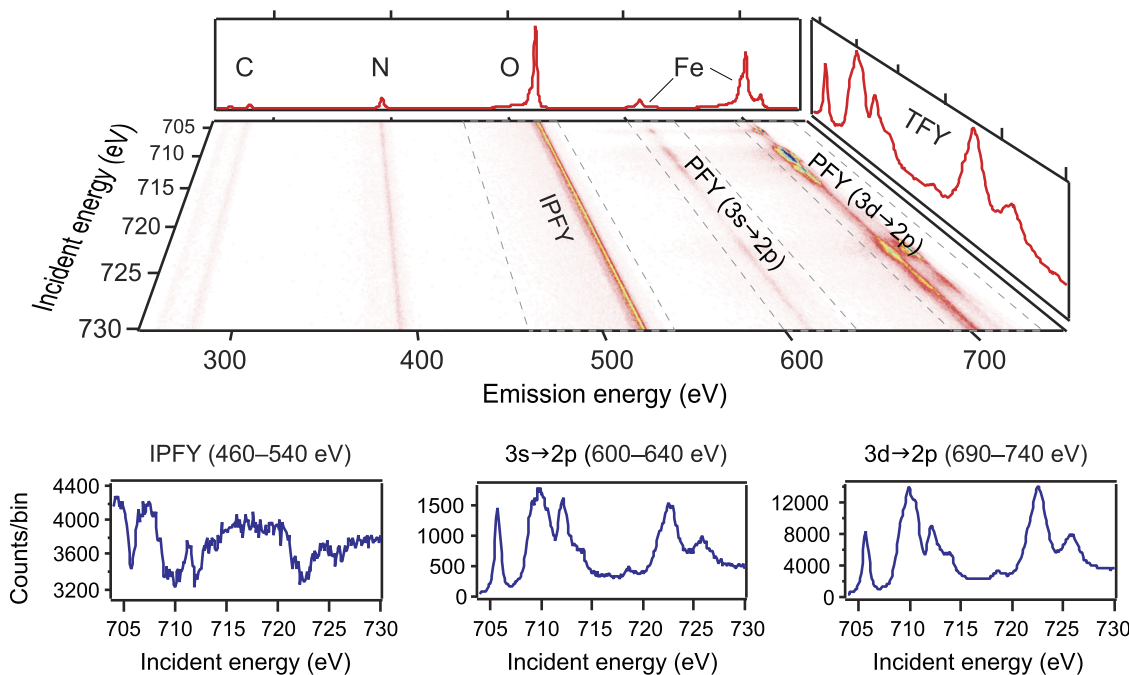
FIG. 6. Resonant inelastic X-ray scattering (RIXS) map of $K_3[Fe(CN)_6]$ obtained by the TES and spectra derived from the RIXS map. The XAS plot based on TFY (top right) is the sum of the RIXS map intensities along the emission-energy axis while the IPFY (bottom left), $3s \rightarrow 2p$ PFY (bottom center), and $3d \rightarrow 2p$ PFY (bottom right) are the sums of the RIXS map within the emission-energy ranges (dashed boxes) of 460–540 eV, 600–640 eV, and 690–740 eV, respectively. The top plot is the sum of the RIXS map along the incident-energy axis. Incident beam energy was swept with 0.1-eV increments.

no added collection time. IPFY is known to provide a spectrum very close to the true absorption spectrum.[42] The IPFY spectrum shown in Fig. 6 was obtained by summing the RIXS data around the K-edge of oxygen instead of the L-edge of the iron. The intensity of the IPFY signal depends on the relative concentration of the oxygen and iron in the sample.

When measuring a radiation-sensitive sample whose oxidation state is easily affected by the incident X-ray beam, it is of critical importance to ensure the measured spectra are free of damage-induced spectral changes.[43] In our RIXS measurements on radiation-damage sensitive samples such as $Fe^{3+}(CN)_6$ (see Fig. 6), we raster-scan the sample using a sawtooth pattern such that the X-ray beam strikes different points of the sample to control the dose received by each particular region of the sample surface. We iteratively adjust the incident radiation dose using the beamline entrance and exit slits and/or by decreasing the measurement time per sample spot location. Ideally, this results in no noticeable difference between TES PFY-XAS spectra obtained throughout the entire measurement process. Radiation damage control in our TES-XES measurements is yet to be implemented.

The dark-count-free nature of the TES is another distinct advantage in XES and XAS/RIXS of extremely dilute samples. In grating-based spectroscopy, in spite of its excellent energy-resolving power, the signal-to-noise ratio (SNR) can be degraded from that of the background-free case due to dark current noise of the photodetector used for counting diffracted photons. Typically, CCD (charge-coupled device) or MCP (microchannel plate) with extremely low

dark current noise are used as the photodetector, but if the signal to be measured is weak compared to the statistical fluctuation of dark counts summed over the region of interest (ROI), the SNR can be non-negligibly degraded. In TES-based spectroscopy, due to its pulse-shape-discrimination capability, any record triggered by a spurious signal such as electromagnetic interference or electrical noise can be rejected. Although cosmic rays and environmental radiation can produce X-ray-like background signals in the TES, their event rate is negligible. Thus, the SNR of a weak signal is simply the square-root of the number of photons collected in the ROI. One exception is nonresonant XES where a strong peak might exist on the high-energy side of ROI, in which case the low-energy tail of the higher-energy peaks would degrade the SNR of the weak peak. For instance, the N spectra in the inset of Fig. 6 is sitting mostly on the low-energy tail of the O-K emission peak. In our TES, the level of the low-energy tail drops to ~0.1% of the height of the high-energy peak at 100 eV below. This kind of background is nonintrinsic to the TES and can be eliminated in future devices as discussed in Sec. III.

VII. CONCLUSION

We have commissioned a new and versatile soft X-ray spectrometer at BL 10-1 of SSRL. The heart of the spectrometer is a 240-pixel array of superconducting Mo/Cu TESs with Bi absorbers. The array offers full-array energy resolution of 1.5 eV FWHM at 500 eV and effective count rates ~2000 cps under normal operating

conditions. This performance is comparable to what was obtained in the laboratory before it was deployed at SSRL. The fully instrumented new spectrometer has already enabled important science experiments on a variety of samples including, e.g., hemoglobin, carbon nanotubes,[39] and Li-ion battery materials.[44]

The relatively large solid-angle and excellent energy sensitivity provided by the new spectrometer make the system especially useful for dilute and/or damage-sensitive samples. In this paper, we have presented results from initial XAS/RIXS and XES measurements on such samples. We also demonstrated that in L-edge XAS/RIXS the broadband spectral coverage of our spectrometer can provide simultaneously measured PFY-XAS spectra for the L-edge in three different modes, namely, the $3d \to 2p$ and $3s \to 2p$ transitions and the IPFY. The combined information from the three spectra can be used to understand and correct for self-absorption or saturation effects that traditional fluorescence yield measurements often suffer from.

The BL 10-1 TES system has also served as a test-bed for other TES spectrometers for synchrotron and X-ray free-electron laser end-stations such as the 240-pixel TES that was recently commissioned at the resonant soft X-ray scattering end-station BL 13-3 of SSRL (to be described elsewhere) and a future, more capable instrument at the liquid-jet end-station of LCLS-II.[45] Our efforts to make the BL 10-1 TES more efficient and user-friendly through improved experimental protocols also benefit these other systems.

In parallel to our efforts at the end-stations, we are also working in the laboratory to develop new TES arrays and read-out systems by incorporating the most recent advances in the TES technology. Through this effort, the BL 10-1 TES array will be upgraded in the near future to have an increased (~50%) collecting area while maintaining or improving energy resolution and per-pixel counting-rate capability (speed) as well as improved detector-response function (reduced low-energy tail). To this end, we have redesigned the individual TES microcalorimeters[46,47] and adopted new sensor-fabrication processes,[35] demonstrating promising initial results. We are also actively developing new microwave-SQUID based multiplexing read-out[48] and supporting electronics[49,50] that would provide ~100 times more bandwidth for both faster sensors and large arrays. A case study on how the new TES spectrometer will perform in the extremely high brightness condition at LCLS-II will be available in a separate publication.[51] These upgrades and developments will greatly enhance the scientific impact of both TES spectrometers at SSRL and the forthcoming one at LCLS-II.

SUPPLEMENTARY MATERIAL

See the supplementary material for the relation between the trigger rate and the X-ray rate and the composition of two different calibration standards.

ACKNOWLEDGMENTS

REFERENCES

[1] F. De Groot and A. Kotani, *Core Level Spectroscopy of Solids* (CRC Press, 2008).

[2] J. Stöhr, *NEXAFS Spectroscopy* (Springer Science & Business Media, 2013), Vol. 25.

[3] R. Mitzner, J. Rehanek, J. Kern, S. Gul, J. Hattne, T. Taguchi, R. Alonso-Mori, R. Tran, C. Weniger, H. Schröder et al., J. Phys. Chem. Lett. **4**, 3641 (2013).

[4] E. Proietti, F. Jaouen, M. Lefèvre, N. Larouche, J. Tian, J. Herranz, and J.-P. Dodelet, Nat. Commun. **2**, 416 (2011).

[5] J.-M. Tarascon and M. Armand, *Materials for Sustainable Energy: A Collection of Peer-Reviewed Research and Review Articles from Nature Publishing Group* (World Scientific, 2011), pp. 171–179.

[6] A. Vailionis, G. Glass, P. Desjardins, D. G. Cahill, and J. Greene, Phys. Rev. Lett. **82**, 4464 (1999).

[7] P. Fons, H. Tampo, A. V. Kolobov, M. Ohkubo, S. Niki, J. Tominaga, R. Carboni, F. Boscherini, and S. Friedrich, Phys. Rev. Lett. **96**, 045504 (2006).

[8] L. Zhao, R. He, K. T. Rim, T. Schiros, K. S. Kim, H. Zhou, C. Gutiérrez, S. Chockalingam, C. J. Arguello, L. Pálová et al., Science **333**, 999 (2011).

[9] K. Siegbahn, C. Nordling, G. Johansson, J. Hedman, P.-F. Heden, K. Hamrin, U. Gelius, T. Bergmark, L. O. Werme, R. Manne, and Y. Baer, *ESCA Applied to Free Molecules* (North-Holland, 1970).

[10] A. Kotani and S. Shin, Rev. Mod. Phys. **73**, 203 (2001).

[11] A. Nilsson and L. G. M. Pettersson, Surf. Sci. Rep. **55**, 49 (2004).

[12] M. Dell'Angela, T. Anniyev, M. Beye, R. Coffee, A. Föhlisch, J. Gladh, T. Katayama, S. Kaya, O. Krupin, J. LaRue et al., Science **339**, 1302 (2013).

[13] P. Wernet, K. Kunnus, I. Josefsson, I. Rajkovic, W. Quevedo, M. Beye, S. Schreck, S. Grübel, M. Scholz, D. Nordlund et al., Nature **520**, 78 (2015).

[14] J. Nordgren and R. Nyholm, Nucl. Instrum. Methods Phys. Res., Sect. A **246**, 242 (1986).

[15] Y.-D. Chuang, Y.-C. Shao, A. Cruz, K. Hanzel, A. Brown, A. Frano, R. Qiao, B. Smith, E. Domning, S.-W. Huang et al., Rev. Sci. Instrum. **88**, 013110 (2017).

[16] A. Hafner, L. Anklamm, A. Firsov, A. Firsov, H. Löchel, A. Sokolov, R. Gubzhokov, and A. Erko, Opt. Express **23**, 29476 (2015).

[17] Z. Yin, H. Löchel, J. Rehanek, C. Goy, A. Kalinin, A. Schottelius, F. Trinter, P. Miedema, A. Jain, J. Valerio et al., Opt. Lett. **43**, 4390 (2018).

[18] F. Marschall, Z. Yin, J. Rehanek, M. Beye, F. Döring, K. Kubiček, D. Raiser, S. T. Veedu, J. Buck, A. Rothkirch et al., Sci. Rep. **7**, 8849 (2017).

[19] T. Tokushima, Y. Horikawa, and S. Shin, Rev. Sci. Instrum. **82**, 073108 (2011).

[20] K. Irwin and G. Hilton, "Transition-edge sensors," in *Cryogenic Particle Detection*, edited by C. Enss (Springer Berlin Heidelberg, Berlin, Heidelberg, 2005), pp. 63–150.

[21] W. B. Doriese, P. Abbamonte, B. K. Alpert, D. Bennett, E. Denison, Y. Fang, D. Fischer, C. Fitzgerald, J. Fowler, J. Gard et al., Rev. Sci. Instrum. **88**, 053108 (2017).

[22] J. Uhlig, W. Doriese, J. Fowler, D. Swetz, C. Jaye, D. Fischer, C. Reintsema, D. Bennett, L. Vale, U. Mandal et al., J. Synchrotron Radiat. **22**, 766 (2015).

[23] R. Qiao, Q. Li, Z. Zhuo, S. Sallis, O. Fuchs, M. Blum, L. Weinhardt, C. Heske, J. Pepper, M. Jones et al., Rev. Sci. Instrum. **88**, 033106 (2017).

[24] J. Bufon, S. Schillani, M. Altissimo, P. Bellutti, G. Bertuccio, F. Billè, R. Borghes, G. Borghi, G. Cautero, D. Cirrincione et al., J. Instrum. **13**, C03032 (2018).

[25] M. O. Krause, J. Phys. Chem. Ref. Data **8**, 307 (1979).

[26] W. B. Doriese, J. Adams, G. Hilton, K. Irwin, C. Kilbourne, F. Schima, and J. Ullom, AIP Conf. Proc. **1185**, 450–453 (2009).

[27] J. Chervenak, K. D. Irwin, E. N. Grossman, J. M. Martinis, C. D. Reintsema, and M. Huber, Appl. Phys. Lett. **74**, 4043 (1999).

[28] J. N. Ullom and D. A. Bennett, Supercond. Sci. Technol. **28**, 084003 (2015).

[29] W. B. Doriese, K. M. Morgan, D. A. Bennett, E. V. Denison, C. P. Fitzgerald, J. W. Fowler, J. D. Gard, J. P. Hays-Wehle, G. C. Hilton, K. D. Irwin et al., J. Low Temp. Phys. **184**, 389 (2016).

[30] C. D. Reintsema, J. Beyer, S. W. Nam, S. Deiker, G. C. Hilton, K. Irwin, J. Martinis, J. Ullom, L. R. Vale, and M. MacIntosh, Rev. Sci. Instrum. **74**, 4500 (2003).

[31] W. B. Doriese, J. A. Beall, W. Duncan, L. Ferreira, G. C. Hilton, K. D. Irwin, C. D. Reintsema, J. N. Ullom, L. R. Vale, and Y. Xu, Nucl. Instrum. Methods Phys. Res., Sect. A **559**, 808 (2006).

[32] K. R. Boyce, M. D. Audley, R. G. Baker, J. J. Dumonthier, R. Fujimoto, K. C. Gendreau, Y. Ishisaki, R. L. Kelley, C. K. Stahle, A. E. Szymkowiak et al., Proc. SPIE **3765**, 741–751 (1999).

[33] J. W. Fowler, B. K. Alpert, W. B. Doriese, J. Hays-Wehle, Y.-I. Joe, K. M. Morgan, G. C. O'Neil, C. Reintsema, D. R. Schmidt, J. Ullom et al., IEEE Trans. Appl. Supercond. **27**, 1 (2016).

[34] J. W. Fowler, B. K. Alpert, W. B. Doriese, Y.-I. Joe, G. C. O'Neil, J. N. Ullom, and D. S. Swetz, J. Low Temp. Phys. **184**, 374 (2016).

[35] D. Yan, R. Divan, L. M. Gades, P. Kenesei, T. J. Madden, A. Miceli, J.-S. Park, U. M. Patel, O. Quaranta, H. Sharma et al., Appl. Phys. Lett. **111**, 192602 (2017).

[36] J. Fowler, B. Alpert, D. Bennett, W. Doriese, J. Gard, G. Hilton, L. Hudson, Y. Joe, K. Morgan, G. O'Neil et al., Metrologia **54**, 494 (2017).

[37] N. Ketabi, T. de Boer, M. Karakaya, J. Zhu, R. Podila, A. M. Rao, E. Z. Kurmaev, and A. Moewes, RSC Adv. **6**, 56721 (2016).

[38] K. Kunnus, L. Li, C. J. Reinhard, K. Ledbetter, K. Kjaer, S. Koroidov, K. Hong, E. Biasin, C. Titus, S. J. Lee et al., "Solvation effects in ultrafast intramolecular electron back-transfer in molecular Fe-based photosensitizers," in XXI International Conference on Ultrafast Phenomena, 2018.

[39] S. Sainio, N. Wester, C. J. Titus, Y. Liao, Q. Zhang, D. Nordlund, D. Sokaras, S.-j. Lee, K. D. Irwin, W. B. Doriese et al., J. Phys. Chem. C **123**, 6114 (2019).

[40] C. J. Titus, M. L. Baker, S. J. Lee, H.-M. Cho, W. B. Doriese, J. W. Fowler, K. Gaffney, J. D. Gard, G. C. Hilton, C. Kenney et al., J. Chem. Phys. **147**, 214201 (2017).

[41] R. Golnak, J. Xiao, K. Atak, I. Unger, R. Seidel, B. Winter, and E. F. Aziz, J. Phys. Chem. A **120**, 2808 (2016).

[42] A. Achkar, T. Regier, H. Wadati, Y.-J. Kim, H. Zhang, and D. Hawthorn, Phys. Rev. B **83**, 081106 (2011).

[43] M. Van Schooneveld and S. DeBeer, J. Electron Spectrosc. Relat. Phenom. **198**, 31 (2015).

[44] S. Li, S.-J. Lee, X. Wang, W. Yang, H. Huang, D. S. Swetz, W. B. Doriese, G. C. O'Neil, J. N. Ullom, C. J. Titus et al., J. Am. Chem. Soc. **141**, 12079 (2019).

[45] D. Li, B. Alpert, D. Becker, D. Bennett, G. Carini, H.-M. Cho, W. Doriese, J. Dusatko, J. Fowler, J. Frisch et al., J. Low Temp. Phys. **193**, 1287 (2018).

[46] J. Hays-Wehle, D. Schmidt, J. Ullom, and D. Swetz, J. Low Temp. Phys. **184**, 492 (2016).

[47] K. Morgan, D. Becker, D. A. Bennet, R. Dorisee, J. D. Gard, K. Irwin, S. J. Lee, D. Li, J. Mates, C. Pappas et al., IEEE Trans. Appl. Supercond. **29**, 2100605 (2019).

[48] J. Mates, D. T. Becker, D. A. Bennett, B. Dober, J. Gard, J. Hays-Wehle, J. Fowler, G. Hilton, C. Reintsema, D. Schmidt et al., Appl. Phys. Lett. **111**, 062601 (2017).

[49] S. W. Henderson, Z. Ahmed, J. Austermann, D. Becker, D. A. Bennett, D. Brown, S. Chaudhuri, H.-M. S. Cho, J. M. D'Ewart, B. Dober et al., Proc. SPIE **10708**, 1070819 (2018).

[50] J. Gard, D. Becker, D. Bennett, J. Fowler, G. Hilton, J. Mates, C. Reintsema, D. Schmidt, D. Swetz, and J. Ullom, J. Low Temp. Phys. **193**, 485 (2018).

[51] C. J. Titus, D. Li, B. K. Alpert, H.-M. Cho, J. W. Fowler, S.-J. Lee, K. M. Morgan, D. S. Swetz, J. N. Ullom, A. Wessels et al., "Count rate optimizations for TES detectors at a femtosecond X-ray laser," J. Low Temp. Phys. (submitted).

12 November 2024 21:09:04